

A phantom system for assessing the effects of membrane lipids on water proton relaxation

Oshrat Shtangel | Aviv A. Mezer

Edmond and Lily Safra Center for Brain Sciences, Hebrew University of Jerusalem, Israel

Correspondence

Aviv Mezer, Edmond and Lily Safra Center for Brain Sciences, Hebrew University of Jerusalem, Israel.
 Email: aviv.mezer@mail.huji.ac.il

Funding information

ISF Grant, Grant/Award Number: 0399306

Quantitative MRI (qMRI) is a method for the non-invasive study of brain-structure-associated changes expressed with measurable units. The qMRI-derived parameters have been shown to reflect brain tissue composition such as myelin content. Nevertheless, it remains a major challenge to identify and quantify the contributions of specific molecular components to the MRI signal. Here, we describe a phantom system that can be used to evaluate the contribution of membrane lipids to qMRI-derived parameters.

We used a hydration-dehydration dry film technique to formulate liposomes that can be used as a model of the bilayer lipid membrane. The liposomes were comprised of the most abundant types of lipid found in the human brain. We then applied clinically available qMRI techniques with adjusted bias corrections in order to test the ability of the phantom system to estimate multiple qMRI parameters such as proton density (PD), T_1 , T_2 , T_2^* and magnetization transfer. In addition, we accurately measured the phantom sample water fraction (normalized PD). A similar protocol was also applied to the human brain *in vivo*.

The phantom system allows for a reliable estimation of qMRI parameters for phantoms composed of various lipid types using a clinical MRI scanner. We also found a comparable reproducibility between the phantom and *in vivo* human brain qMRI estimations.

To conclude, we have successfully created a biologically relevant liposome phantom system whose lipid composition can be fully controlled. Our lipid system and analysis can be used to measure the contributions to qMRI parameters of membrane lipids found in the human brain under scanning conditions that are relevant to *in vivo* human brain scans. Such a model system can be used to test the contributions of lipidomic changes in normal and pathological brain states.

KEY WORDS

lipids, phantom, quantitative-MRI, reproducibility

Abbreviations: B_1^- , receive coil inhomogeneity; B_1^+ , transmit coil inhomogeneity; CV, coefficient of variation; D₂O, deuterium oxide; DDW, double distilled water; DLS, dynamic light scattering; EMC, echo-modulation curve; EPI, echo-planar imaging; FA, fractional anisotropy; FLASH, fast low angle shot; FoV, field of view; MD, mean diffusivity; MT, magnetization transfer; MT_{norm}, normalized magnetization transfer; MTV, macromolecule tissue volume; GS, gold standard; PBS, Dulbecco's phosphate buffered saline; PC, phosphatidylcholine; PD, proton density; PI, phosphatidylinositol; PS, phosphatidylserine; qMRI, quantitative MRI; SEIR, spin-echo inversion recovery; Spg, sphingomyelin; SPGR, spoiled gradient echo; STD, standard deviation; TEM, transmission electron microscopy; VFA, variable flip angle; WF, water fraction.

1 | INTRODUCTION

Quantitative MRI (qMRI) analysis allows for the study of the human brain using parametric maps that have measurable units such as relaxation times (measured in seconds). These qMRI maps enable a reliable comparison of brain structure across different time points and different MRI scanners, making it possible to assess normal brain development, as well as pathological conditions.¹

Different qMRI parameters have been associated with a number of biological sources. For example, changes in myelination levels are reflected by alterations in T_1 , magnetization transfer (MT), and T_2 .²⁻⁵ Furthermore, the iron content and water fraction (WF) of cellular compartments are also thought to influence the qMRI parameters.^{6,7} Nevertheless, it still remains a major challenge to localize and quantify the contribution of a specific biochemical environment to the MRI signal *in vivo*. Therefore, in the qMRI field, considerable effort has been invested in building phantoms that mimic the natural environment of the human brain. Such phantoms permit insights into potential biological sources of the signal while maintaining strict control over the precise content of the phantom.^{8,9} A critical advantage of such phantoms is that they allow the study of the consistency and reliability of qMRI parameters in time and space. The main objective of this work was to establish an experimental system that could describe the contribution of membrane lipids to qMRI parameter mapping.

The human brain is comprised mainly of water (70–80%), proteins (8–11%) and lipids (5–15%). The distribution of these molecules varies between brain regions, across lifespan, and in different pathological states.¹⁰⁻¹⁴ There are five major groups of lipids in the brain: phospholipids (main component), cholesterol, and three types of glycolipid (cerebrosides, gangliosides, and sulfatides). Most of the lipids in the human brain are found in cell membranes, where they are involved in many important biological circuits and cellular functions.¹⁵ Lipids are known to strongly affect the contrast of brain qMRI maps, a claim recently supported by experiments using lipid-clearing techniques.¹⁶

Early NMR studies indicated that myelin, which is mainly composed of lipids, has a strong effect on T_1 and MT qMRI parameters. This was initially attributed to the interaction between water protons and cholesterol in myelin membranes,¹⁷ although later studies showed that other lipids and macromolecules, such as proteins, also influence the magnetic relaxation of water protons.¹⁸⁻²⁰ Additional studies focused on the sensitivity of qMRI parameters to the lipid bilayer structure and revealed the effect of different surface groups and of pH.²¹⁻²³ Nevertheless, there remains a need for a systematic quantification of the effect of lipids using the current qMRI mapping approaches that are used for *in vivo* brain imaging on a clinical scanner.

This study describes a phantom system designed to assess the contribution of various membrane lipids to qMRI parameters using a clinical human scanner. We created liposomes with lipids that are similar to the most abundant types found in the human brain.²⁴ We choose five lipid types: phosphatidylcholine (PC), sphingomyelin (Spg), and phosphatidylserine (PS) to represent phospholipids, cholesterol to represent the sterol group, and phosphatidylinositol (PI) to represent the glycolipids.²⁵

We validated the phantom system and tested its reliability. Importantly, the phantom's qMRI scanning and fitting procedures are based on previous human experimental protocols^{25,26}. Here, we verified the protocol reproducibility on both lipid phantoms and a human brain *in vivo*. Our results demonstrate that the lipid membrane qMRI parameters WF, T_1 , T_2 , and MT can be estimated with high reproducibility. We propose that this system can serve as a tool to examine the contribution of membrane lipid composition to qMRI parameters.

2 | METHODS

2.1 | Phantom samples

2.1.1 | Sample preparation

The phantom system is based on liposomes that model cellular membranes. We used phospholipids to prepare the liposomes using the hydration-dehydration dry film technique.²⁷

The following highly purified and lyophilized lipids were used in this protocol (one or more in each experiment): L- α -phosphatidylcholine (PC), L- α -phosphatidylinositol (PI), and cholesterol (Sigma-Aldrich), and DO-phosphatidylserine 18:1/18:1 (PS) and E sphingomyelin (Spg) (LIPOID).

The lipids were dissolved in ethanol, methanol, or chloroform over a hot plate and vortexed. Next, the solvent was removed by vacuum-rotational evaporation to create a dry film. Dulbecco's phosphate buffered saline (PBS), without calcium and magnesium (Biological Industries, Kibbutz Beit-Haemek, Israel), was added to the dry film in order to obtain a final sample, by volume, of 25–30% liposomes, and 70–75% water, at a pH similar to physiological conditions (pH ~ 7.5). The sample was then stirred on a hot plate at 65°C for 2.5 h to allow the lipids to achieve their final liposome conformation. Samples were further diluted with PBS to obtain preparations with the liposome concentration in the PBS range from 5 to 30%, by volume, for a final sample volume of 1.5 mL in a 4 mL square polystyrene cuvette with a lid, 12.5 mm × 12.5 mm × 45 mm (light path: 10 mm ± 0.05 mm). Cuvettes were glued to a polystyrene box, which was then filled with ~1% SeaKem agarose (Ornat Biochemical, Rehovot, Israel) and ~0.0005 M Dotarem (gadoterate meglumine, Guerbet, Paris, France) dissolved in double distilled water (DDW) (Figure 1A). The purpose of the agar was to stabilize the cuvettes and to minimize air-cuvette interfaces. The agar with Gd (agar-Gd) also creates a uniform volume

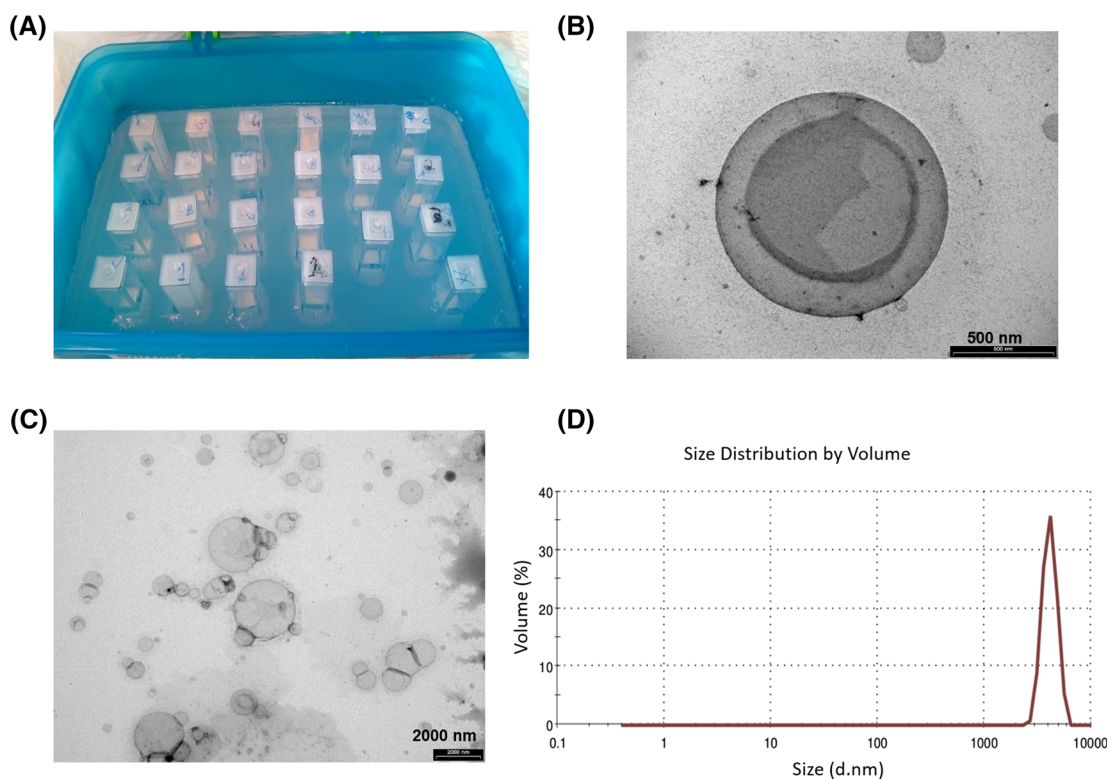


FIGURE 1 The phantom system. A, the phantom box: A plastic container ($22\text{ cm} \times 13\text{ cm} \times 9\text{ cm}$) containing 23 cuvettes filled with mixtures of liposomes and water, surrounded by homogeneous agar-Gd gel. Some of the cuvettes are pure water samples that are used for WF normalization. B, C, liposome formation: TEM images of liposomes. B, the image centre shows a single liposome about $1\text{ }\mu\text{m}$ in diameter. C, the zoomed-out image shows a wide distribution of liposome sizes. Overlap between liposomes is due to the imaging technique. D, example of liposome size distribution from DLS measurements

surrounding the cuvettes with a low T_1 value. This uniform agar-Gd volume was used for the bias correction stage of the analysis (see Section 2.3.1). Fresh agar was prepared for each scan except for the scan-rescan experiments. To estimate the qMRI parameters without lipids, we also prepared water-based samples using PBS and DDW.

Finally, to test the accuracy of the WF estimations, we conducted a separate experiment without lipids, where DDW (H_2O) and deuterium oxide (D_2O) were mixed in different ratios.

2.1.2 | Liposome volume estimation

We estimated the volume of 1 g of a given phospholipid in water based on the molar mass and the combined volume of the head group and the tail (methylene groups) of a single lipid molecule. Different lipid types vary in volume due to differences in the polar head groups and the tail composition.^{28–30} The volume estimations used to calculate the lipid volume of each sample were as follows: the estimated volumes of 1 g PC/PC:cholesterol, PS, Spg, and PI are 0.976 mL, 0.887 mL, 1.000 mL, and 1.391 mL, respectively. For mixtures with cholesterol, we assumed the cholesterol volume to be negligible according to the free-space theory.³¹

2.1.3 | Transmission electron microscopy (TEM) and dynamic light scattering (DLS) measurements

TEM was used in order to verify and visualize the formation of liposomes. Samples of 10% liposomes by volume were diluted by a factor of 10^2 followed by centrifugation. The supernatant was harvested and diluted by a factor of 10. Final samples were negatively stained with uranyl acetate.³²

In a separate experiment, the size distribution of the prepared liposomes was estimated by DLS (Malvern Zetasizer)³³ measurements of 10% samples diluted by a factor of 10^3 .

2.1.4 | Image acquisition

The phantom system scan protocol was designed to resemble a human brain scan. Phantom samples were scanned in a Skyra (Siemens, Erlangen, Germany) 3 T MRI scanner with a 32 channel receive head-coil. The phantom was kept in the magnet room for 20 min before the scan started in order to achieve thermal equilibrium. The magnet room was kept at a constant temperature of ~18°C.

Spoiled gradient echo (SPGR)

For T_1 and proton density (PD) mapping, images were acquired using a fast low angle shot (FLASH) sequence with four flip angles, $\alpha = 4^\circ, 8^\circ, 16^\circ, 30^\circ$, $T_E = 3.91$ ms, $T_R = 18$ ms, field of view (FoV) of 205 mm^2 , and voxel size of $1.1\text{ mm} \times 1.1\text{ mm} \times 0.9\text{ mm}$. The same sequence was repeated with a higher resolution of $0.6\text{ mm} \times 0.6\text{ mm} \times 0.5\text{ mm}$ with three averages.

For MT mapping and T_2^* contribution estimations, additional images were acquired using a prototype MT FLASH sequence with $T_R = 23$ ms, $T_E = 1.93, 4.46, 6.99, 9.52, 12.05, 14.58$ ms, flip angle = 6° , FoV of 205 mm^2 , and voxel size of $1.1\text{ mm} \times 1.1\text{ mm} \times 0.9\text{ mm}$. The same sequence was repeated with a higher resolution of $0.6\text{ mm} \times 0.6\text{ mm} \times 0.5\text{ mm}$ with three averages.

For the MT analysis, an initial image without an MT pulse was followed by 14 images with RF offsets = [100, 200, 300, 400, 500, 600, 700, 800, 900, 1000, 2000, 4000, 50 000Hz], with MT flip angle of 220° , spoiler moment = $25\,000\,\mu\text{s mT/m}$, and MT pulse duration = 4000 ms. This sequence follows earlier work by Gunther Helms et al.⁴

Spin-echo inversion recovery (SEIR)

For T_1 calibration, single-slice images were acquired using an SEIR sequence with adiabatic inversion pulse and inversion times of $T_I = 2000, 1200, 800, 400, 50$ ms, $T_R = 2540$ ms, $T_E = 73$ ms, FoV of 222 mm^2 , and voxel size of $1.2\text{ mm} \times 1.2\text{ mm} \times 2\text{ mm}$.

Spin echo

For T_2 mapping, images were acquired with multi-spin-echo sequences with 15 echo times $T_E = 10.5, 21, 31.5, 42, 52.5, 63, 73.5, 84, 94.5, 105, 115.5, 126, 136.5, 147$, and 157.5 ms, $T_R = 4940$ ms, FoV of 207 mm^2 and voxel size of $1.1\text{ mm} \times 1.1\text{ mm} \times 1.1\text{ mm}$.

Echo-planar spin echo

Diffusion imaging was acquired using a diffusion-weighted spin-echo (echo-planar imaging, EPI) sequence with isotropic 1.7 mm resolution. Diffusion weighting gradients were applied in 32 directions and the strength of the diffusion weightings was set to $b = [500, 1000, 2000]\text{ s/mm}^2$. $T_E = 95$ ms, $T_R = 9.823$ s, $\delta = 29.3$ ms, $\Delta = 43.5$ ms. The data includes two non-diffusion-weighted images ($b = 0$).

Gradient echo (GRE)

For B_0 measurements, images were acquired with two echo times = [4.92, 7.38], $T_R = 425$ ms, flip angle of 45° and voxel size of size of $2.9\text{ mm} \times 2.9\text{ mm} \times 3.0\text{ mm}$.

2.2 | Human subjects

2.2.1 | Image acquisition

Five subjects (ages 24–31 years) were scanned twice; four of them were scanned with one week between the two scans and one subject was scanned with six months between the two scans. The Helsinki Ethics Committee of Hadassah Hospital, Jerusalem, Israel, approved the experimental procedure. Written informed consent was obtained from the participant prior to the procedure.

SPGR

For T_1 and PD estimations we used 3D spoiled gradient-echo (FLASH) images acquired with different flip angles ($\alpha = 4^\circ, 10^\circ, 20^\circ$, and 30°). Each image included five equally spaced echoes ($T_E = 3.34\text{--}14.02$ ms) and the T_R was 19 ms. The scan resolution was 1 mm isotropic.

For MT analysis, we used an additional MT off-resonance pulse. The flip angle was 10° , the T_E/T_R was $3.34/20$ ms. The envelope shape was Gaussian, bandwidth of 375 Hz with time product of $5120\,\mu\text{s}$, MT flip angle of 500° , pulse duration of $9984\,\mu\text{s}$, and frequency offset of 1200 Hz.

SEIR

For calibration, we acquired an additional spin-echo inversion-recovery scan with an EPI read-out (SEIR-epi). This scan was done with a slab-inversion pulse and spatial-spectral fat suppression. For SEIR-epi, the T_E/T_R was $49/2920$ ms. The T_I were 200, 400, 1200, and 2400 ms. We used 2 mm in-plane resolution with a slice thickness of 3 mm. The EPI readout was performed using $\times 2$ acceleration.

Spin echo

Multi spin-echo images were acquired, with 10 equally spaced spin echoes between 12 ms and 120 ms. The T_R was 4.21 s. The scan resolution was 2 mm isotropic.

2.2.2 | Image processing

We used MATLAB³⁴ to process the data. Manual segmentation of the areas of interest (ROI, agar, and sample cuvettes) was done using ITKsnap³⁵. Segmentation was designed to minimize both sample-plastic and sample-air interfaces. To estimate the qMRI parameters of each segmented cuvette (ROI), the median and the median absolute deviation were calculated.

The code is available at https://github.com/MezerLab/mrQ_Phantoms.

2.3 | Quantitative maps

2.3.1 | Phantoms

 T_1 mapping and bias corrections

We estimated T_1 using the variable flip angle³⁶ (VFA) approach (Equation (1), spoiled gradient-echo signal equation), which is commonly used for human brain quantitative T_1 mapping.

$$\text{Signal} = M_0 \times \frac{\sin \alpha (1 - \exp(-\frac{T_R}{T_1}))}{1 - (\cos \alpha) \exp(-\frac{T_R}{T_1})}, \text{ where } M_0 = PD' \times \text{gain} \times \exp\left(\frac{-T_E}{T_2^*}\right) = \gamma \times PD \times \text{gain} \times \exp\left(\frac{-T_E}{T_2^*}\right) \quad (1)$$

PD' is PD multiplied by the proportional constant γ , gain is the receiver coil inhomogeneity (B_1^-), T_E is the echo time, T_R is the repetition time, M_0 is the steady-state magnetization, α is the flip angle and T_2^* is the effective transverse relaxation constant.

The VFA T_1 mapping contains biases resulting from inhomogeneity in the excitation RF pulse (B_1^+). This inhomogeneity leads to spatial uncertainty regarding the true flip angle used in different positions in space. This error can be described as the percent difference between the nominal and the true flip angle value:

$$B_1^+ \text{ error} = \frac{\alpha_{\text{nominal}}}{\alpha_{\text{true}}} \quad (2)$$

B_1^+ is the transmit coil inhomogeneity, α_{nominal} is the flip angle assumed to be used, and α_{true} is the true flip angle used.

In order to account for the B_1^+ inhomogeneity (excitation bias) in the phantom VFA T_1 map, we modified a correction method that was previously described for the human brain.^{24,26} In this approach the VFA T_1 map is calibrated with a SEIR T_1 map, which is considered the gold standard sequence for estimating T_1 (GS-T1).³⁷ This analysis is based on adaptations of mrQ³⁸ and VISTA lab³⁹ software. In brief, we used the fact that the agar-Gd filling the box around the samples is homogeneous and has a constant T_1 value. We estimated the agar-Gd T_1 value (GS-T1) using the algorithm reported by Barral et al.³⁷ Finally, we used this GS-T1 value and the assumption that B_1^+ inhomogeneity is smooth in space to correct for the B_1^+ inhomogeneity in the VFA T_1 map.

The analysis pipeline is described below.

1. We manually segmented the agar-Gd in the GS-T1 map and averaged its T_1 values across the measured slice. This GS-T1 value is assumed to be accurate and free of bias.
2. We manually segmented the agar-Gd in the 3D FLASH spoiled gradient-echo volume.
3. We fixed the bias-free GS-T1 value along the agar-Gd ROI in the 3D FLASH volume and used Equation (1) and Equation (2) to calculate the flip angle error (B_1^+) numerically. This produced an estimate of the B_1^+ error values in each agar-Gd voxel in the FLASH volume.
4. Assuming that B_1^+ is smooth in space, we interpolated and extrapolated the B_1^+ values to the whole volume and generated a full B_1^+ map using a low-order polynomial.
5. Using the B_1^+ bias map, we used Equation (1) to calculate excite-bias free T_1 and M_0 values for the entire volume, including the cuvette samples.

WF mapping

In order to evaluate the WF in the phantom system we modified an existing method previously used for the human brain *in vivo*.²⁶ In this approach, PD' is disentangled from M_0 (Equation (1)). First, we assume that the short T_E used allows us to neglect contributions from T_2^*

(Equation (2); see also Figure 10). We assumed that M_0 is proportional to PD' and the receive coil gain inhomogeneity (B_1^-) (Equation (2)). Next, we can remove the spatial inhomogeneity. Finally, we normalize PD' against a pure water sample. This was done using the following steps.

- Assuming that the agar-Gd's PD values are homogeneous across space, any smooth variation detected in the agar-Gd ROI in the phantom M_0 volume must be due to receive (B_1^-) inhomogeneity. The estimated bias was calculated locally in the agar-Gd ROI by using low-order polynomials. These local bias estimations were combined to obtain the receive inhomogeneity map over the whole volume.
- PD' was obtained from M_0 and the calculated B_1^- inhomogeneity map using Equation (1) ($PD' = M_0/\text{gain}$).
- In each phantom, we included several pure water/buffer sample cuvettes in different locations in space. These samples were used to calibrate the PD' map, such that the average PD value of the water cuvettes was equal to unity. Applying this calibration to the PD' map resulted in an estimated WF map, with normalized values between zero and unity.

Importantly, after removing the coil gain from M_0 , the values obtained are only proportional to PD ($PD' = \gamma PD$). Therefore, the values need to be scaled against a known sample. Thus, we performed normalization to the PD' values against a pure water sample. Ignoring the neglectable contribution on phospholipid proton to the MRI signal with the (relatively long) T_E values used.⁴⁰ We named the measure obtained a WF map. To calculate the non-water lipid fraction (equivalent to the lipid and macromolecule tissue volume (MTV) term in the human brain),²⁶ we subtracted the WF value of each sample from the WF value of pure water (ie, $MTV = 1 - WF$).

To approximate T_{2^*} contributions in the PD estimations (see Equation (1)), we compared the PD' estimate for $T_E = 1.93$ with PD' for $T_E = 3.9$. To calculate the PD' dependence on T_E (PD^*) we used the estimated parameters (ie T_1 , B_1^+ and B_1^-) from Equation (1) and Equation (2) (see above) and calculated PD^* at the different T_E values:

$$PD^*_{T_E} = \text{signal}_{T_E} / \left(\text{gain} \frac{\sin\alpha(1 - \exp(-\frac{T_R}{T_1}))}{1 - (\cos\alpha)\exp(-\frac{T_R}{T_1})} \right) \quad (3)$$

Here again the WF value was obtained by normalizing the PD^* value of the lipid samples to the PD^* value of the water samples.

T_2 mapping

The T_2 relaxation constant was estimated from a multi-spin-echo sequence using the echo-modulation curve (EMC) algorithm.⁴¹ This algorithm assumes that the actual signal received is not a perfect decaying exponent. Instead, it estimates T_2 values by simulating the Bloch equation and utilizing a lookup table of the parameters used in the sequence.

MT mapping

An SPGR sequence with multiple off-resonance RF pulses was used in order to estimate the ratio $MT_{\text{on}}/MT_{\text{off}}$ (termed MT_{norm} for simplicity).²² Having compared the data for three MT off-resonance flip angles, we chose to work with the MT flip angle of 220° and the 700 Hz off-resonance pulse, where the direct effect of water appears minimal. This can be seen in Figure 2, where the z-spectrum of water reaches a value of approximately 1 at 700 Hz (black arrow).

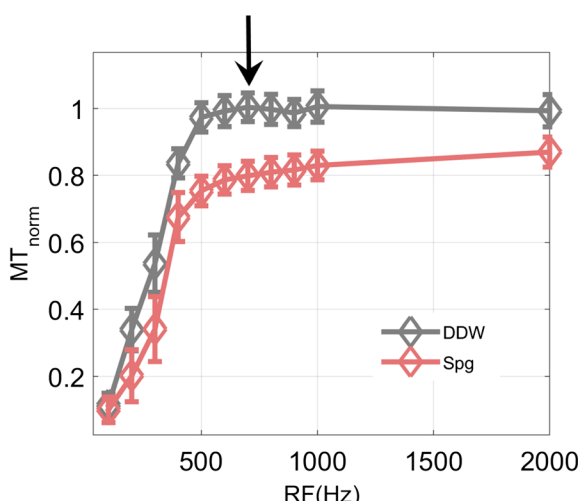


FIGURE 2 Choosing the RF frequency offset for the MT experiments. Examples of MT_{norm} z-spectra for water (DDW) and a liposome sample of sphingomyelin (Spg), showing mean \pm STD for each sample. For further MT_{norm} scans and analysis we chose an RF offset frequency of 700 Hz (black arrow), for which the direct effect of water is minimal (ie, the MT_{norm} value of DDW is closest to 1). The Spg spectrum is shown as an example of a liposome spectrum

Diffusion tensor imaging (DTI)

Diffusion tensor analysis was done using the VISTASOFT toolbox.³⁹ Corrections for the eddy-current-induced distortions were implemented in the VISTASOFT toolbox. With the DTI analysis we calculate the fractional anisotropy (FA) and mean diffusion (MD) maps.⁴²

Importantly, the EPI-based sequence is suboptimal for this phantom system. We note that the EPI diffusion images are highly distorted in our samples (Figure S1). Therefore, we manually and carefully segmented the samples.

B_0 field mapping

To calculate the B_0 field map two gradient echo magnitude images at different echo times and a phase difference image were acquired. We used the FSL software⁴³ to calculate the B_0 field map (FUGUE tool).

2.3.2 | Human subjects

MTV and T_1 mapping

Whole-brain MTV and T_1 maps, together with bias correction maps of transmit (B_1^+) and receive (B_1^-) inhomogeneity, were computed as described by Mezer et al.^{25,26} The analysis pipeline for producing unbiased T_1 and MTV maps is an open-source MATLAB code (available at <https://github.com/mezera/mrQ>).

T_2 mapping

Whole-brain T_2 maps were computed as described by Ben-Eliezer et al,⁴¹ by implementing the EMC algorithm.

MT_{norm} mapping

Whole-brain MT_{norm} maps were computed as described by Henkelman et al.²²

In order to compare between the repeated human scans we used the ANTS software package⁴⁴ to register the maps.

3 | RESULTS

In this study, we developed and evaluated a liposome phantom system and analysis software for qMRI mapping (Figure 1). Our objective is to provide an experimental system that can be used for studying the effect of biologically relevant membrane lipids on qMRI measurements in clinical scanners.

3.1 | Liposome samples

Figure 1B and 1C shows TEM images of the liposomes, with the lipids organized in spherical membrane structures as expected, indicating the success of the manufacturing process. A typical size distribution of the liposomes with an average diameter of 1–10 μm is shown in Figure 1D.

3.2 | Establishing an experimental system for qMRI of the phantom

3.2.1 | Homogeneity and stability of the agar-Gd

The liposome samples are contained in plastic cuvettes that are embedded in agar with Gd ions (agar-Gd).

The GS-T1 analysis indicated that the agar-Gd ROI was homogeneous and gave stable results in space (up to 3.5% change in each scan; $N = 31$ scans), with T_1 values of 421 ± 63 ms (mean \pm standard deviation, STD) across all voxels and scans.

In each scan the agar-Gd ROI is used to estimate both receive and transmit bias fields by assuming the ROI is a homogeneous area. Figure 3 shows a slice through the phantom array (Figure 1), presenting maps of the qMRI parameters WF, T_1 , T_2 and MT_{norm} . Figures S2–S5 present the maps of the qMRI parameters WF, T_1 , T_2 and MT_{norm} for several slices of the phantom. Importantly, while our bias corrections are calculated only on the agar-Gd ROI, they can be extended to correct for instrumental biases in the entire volume of the system, including the lipid sample ROIs.

Figure 4A shows a typical distribution of VFA T_1 values for agar-Gd before and after the B_1^+ correction. Figure 4B presents a typical B_1^+ bias map. Figure 4C and 4D are T_1 maps before and after the B_1^+ correction respectively. A typical receive gain bias is shown in Figure 4E. Figure 4F

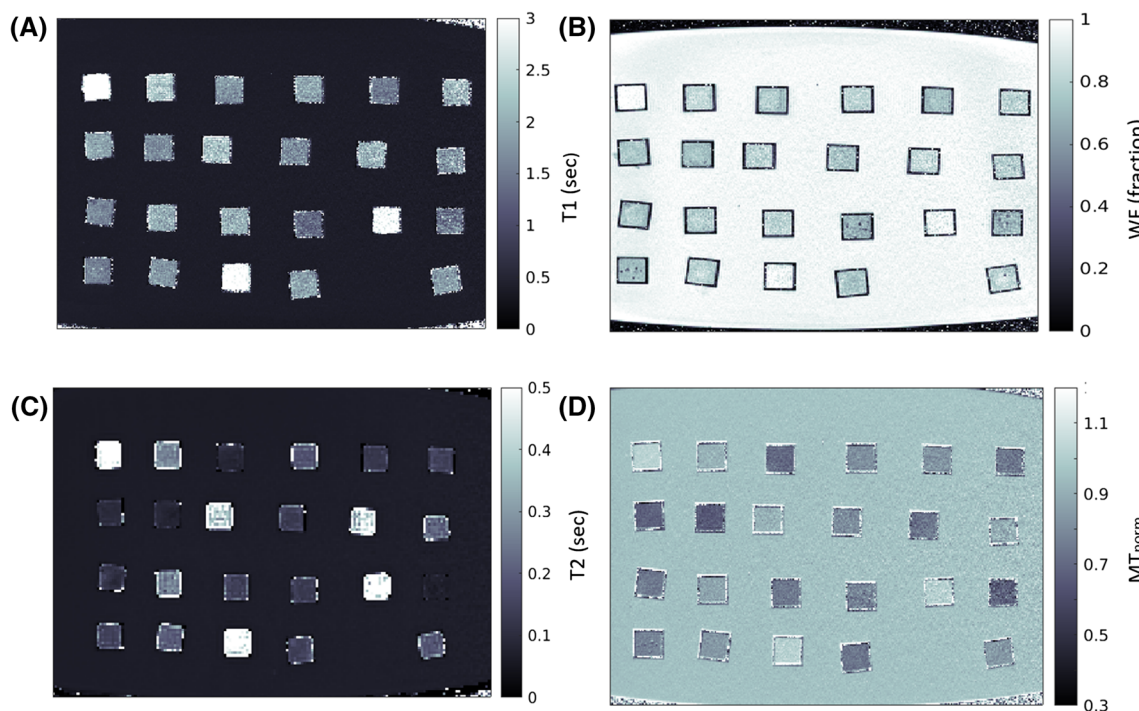


FIGURE 3 Quantitative MRI maps. A-D, a slice through the phantom array shown in Figure 1 indicating T_1 , WF, T_2 and MT_{norm} maps respectively. The cuvette borders can be seen in black (B), while cuvettes have different characteristic values, reflecting liposome content and water fraction, the agar-Gd gel area around the cuvettes is a relatively homogeneous area in all qMRI maps

shows a corrected PD' map. These corrections were designed to remove the biases from the T_1 and PD' estimations. Summarizing multiple experiments ($N = 31$), the average STD of the agar-Gd ROI in space was 2.7% for VFA T_1 and 1.7% for WF. Notably, the EMC T_2 mapping algorithm, which includes a built-in bias correction, generated a stable T_2 in space (median value of 0.07 s, $N = 30$), with a typical STD of 2% of the signal. Similarly, the MT_{norm} parameter, which is defined as the MT_{on} to MT_{off} ratio, also had a small STD of 1.75% in space (median value of $MT_{norm} = 0.95$, $N = 30$).

Importantly, in agreement with earlier results⁴⁵ there is greater noise in samples with greater WF (Figure 5). Nevertheless, repeated measurements of the relaxation of water in multiple experiments ($N = 30$) showed stable results (mean \pm STD: T_1 , 3.84 ± 0.89 s; T_2 , $\geq 0.66 \pm 0.05$ s; MT, 0.99 ± 0.02). It is important to note that we measured T_2 using a range of T_E values that are too short for measuring the true T_2 of water (maximal $T_E = 157$ ms). This T_E range is optimal for measurement of shorter T_2 values such as in the brain grey and white matter areas as well as in our lipid phantoms.⁴¹

To further examine the stability of the system we plot the water sample T_1 values as a function of scanning date over 1.5 years of scanning (Figure S6). While we find relatively constant T_1 values through the year we do note a small but visible periodic change that might be attributable to small temperature differences⁴⁶ or other inconsistencies in the scanner environment.

3.2.2 | Homogeneity, stability and consistency of the liposome qMRI maps

To test the reproducibility of the qMRI liposome phantom measurements, we compared multiple scans of the same liposome samples taken on different days (between 2 and 15 days apart). We found remarkable consistency in WF, T_1 , T_2 and MT_{norm} estimates across scans (Figure 5), with a high coefficient of determination ($R^2 = 0.93, 0.90, 0.93$ and 0.85 respectively, $N = 78$). Finally, one sample was scanned three times over 15 days and showed similar levels of consistency (Figure S7).

Next, we tested the distribution of values within each sample ROI. Figure 6 shows the distribution of values within a sample of each slice. The distribution of values represents the noise measurement in our sample given the scanning parameters and measurement resolution. When comparing the median value across slices within the cuvette along the z-direction (the long axis of the cuvette) we find no systematic variability. We used a one-way ANOVA test to rule out any outlier slices in space on a randomly selected subset of the cuvettes. In addition, we also estimated the SNR of our WF estimations according to Chang et al⁴⁵ (SNR₀, calculated as M_0 divided by the signal STD) for each of the samples. We found $SNR_0 = 206 \pm 87$ in the SPGR measurement. Furthermore, we also estimated the median coefficient of variation (CV) across all samples.

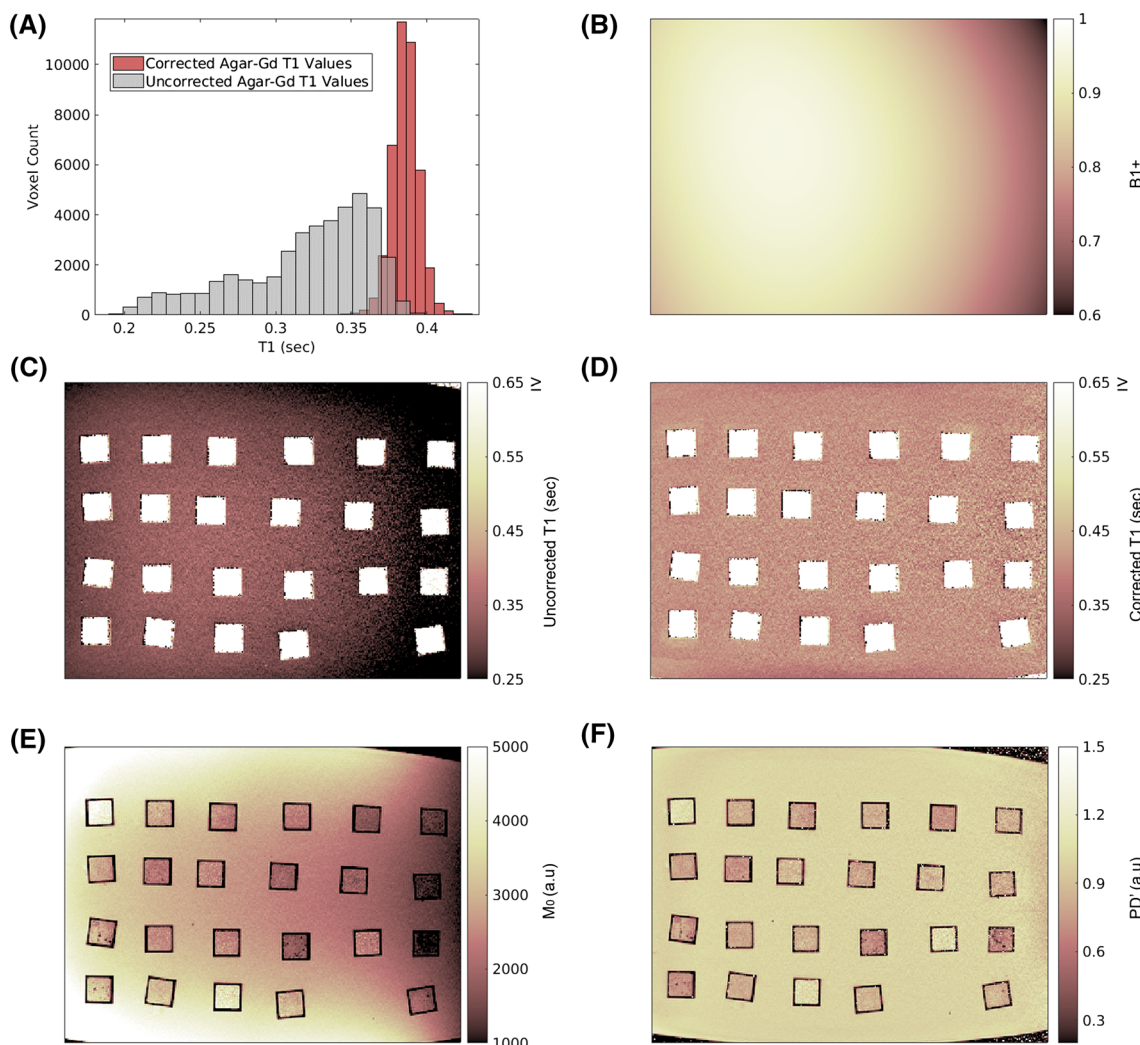


FIGURE 4 B_1^+ inhomogeneity and B_1^- inhomogeneity corrections based on the agar-Gd areas. A, distribution of T_1 values of the agar-Gd ROI estimated by the VFA technique before and after the B_1^+ correction. As expected, the distribution is much narrower after the correction. B, a typical B_1^+ inhomogeneity estimation with a peak in the Centre of the volume (brighter shades in the Centre and darker shades at the periphery). C, T_1 map before the B_1^+ correction. D, T_1 map after the B_1^+ corrections. Values above 0.65 s are clipped for visualization purposes. E, M_0 map, where $M_0 = PD \times \text{gain}$. The receive coil gain inhomogeneity (B_1^-) can be seen across the image (yellow to blue shades). F, PD map after the removal of the receive coil gain inhomogeneity

We calculated the mean CV of our samples (the STD of the sample divided by its mean) for WF (0.07), T_1 (0.09), T_2 (0.03) and MT_{norm} (0.05). We also estimated the CV for the scan-rescan experiments. We calculated the median and STD values of the samples across days ($CV_{\text{scan-rescan}}$). The average $CV_{\text{scan-rescan}}$ across the samples was 0.02 (WF), 0.04 (T_1), 0.06 (T_2) and 0.02 (MT_{norm}).

In addition, we tested the contribution of possible B_0 inhomogeneity to our estimations. To test the B_0 effect, we scanned and rescanned the phantom in two positions within the magnet while also scanning B_0 -weighted field images. We compared the B_0 field maps of each position. Next, we compared the T_1 , T_2 , MT and WF values for identical samples that were placed at different positions in space in each scan. Figure S8A shows T_1 maps for the two scans; the second scan is a 180° flip from the first scan. Figure S8B is the B_0 field maps for the two scans. Figure S8C is a comparison of the T_1 , WF, T_2 and MT values for each sample between the two positions. While B_0 is different in space, the qMRI values remain stable in the two orientations (values around the identity line).

3.2.3 | Stability of parameter estimations on human subjects

In order to compare the qMRI parameters of lipid phantoms and of in vivo human scans, we looked at values for T_1 , T_2 , WF and MT_{norm} . We find that the lipid phantom has a similar range of qMRI values to the human brain. We also compared the reproducibility in human qMRI scans to that

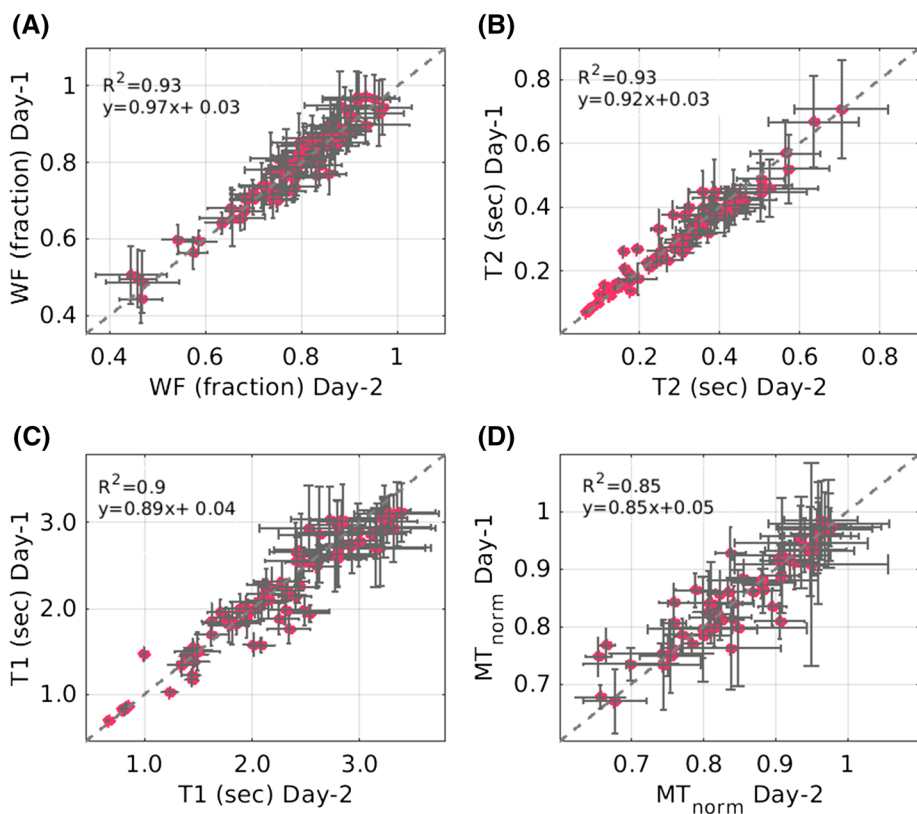


FIGURE 5 Reproducibility of the qMRI parameters in phantom experiments. qMRI parameters were fitted for two scans of the same lipid samples on different days. A-D, WF, T_2 (s), T_1 (s) and MT_{norm}, respectively. Values estimated on different days were highly reproducible. Each point represents one lipid sample. Error bars correspond to median absolute deviation. Values are around the identity line (dashed line; see inset for linearity equation)

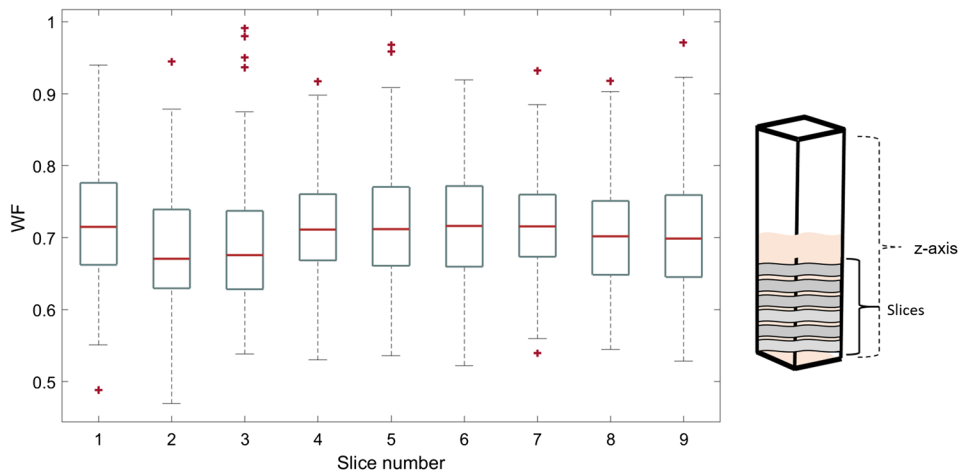


FIGURE 6 Homogeneity of slices across a cuvette. Profile of WF values across slices of a single liposome-containing cuvette. Each bar represents the median and the 25% and 75% percentiles on WF values of one slice. The whiskers extend to the most extreme data points (not including outliers). Red crosses represent outlier values. It is clear that there is no systematic gain in WF values across slices. The right-hand inset is an illustration of a cuvette z-axis and the slices across it

obtained with the phantoms. We scanned the same human subjects ($N = 5$) on two different days (Figure 7). The values for T_1 , T_2 , WF and MT_{norm} were highly reproducible, with a coefficient of determination R^2 of 0.77, 0.69, 0.8 and 0.84 respectively, and with the corresponding values centred around the identity line (with an intercept close to zero).

We also estimated CV_{scan-rescan} for each voxel in human brain scans. The average CV_{scan-rescan} values are 0.03 (WF), 0.06 (T_1), 0.09 (T_2) and 0.05 (MT_{norm}).

3.3 | Validity of the WF estimations

There is great value in validating the WF MRI base estimations. An analytical estimation of phospholipid volume provided an opportunity to verify it. The calculated lipid volume (see Section 2.1.2) showed good agreement ($R^2 = 0.87$, Figure 8B) with the qMRI-based estimate of lipid fraction

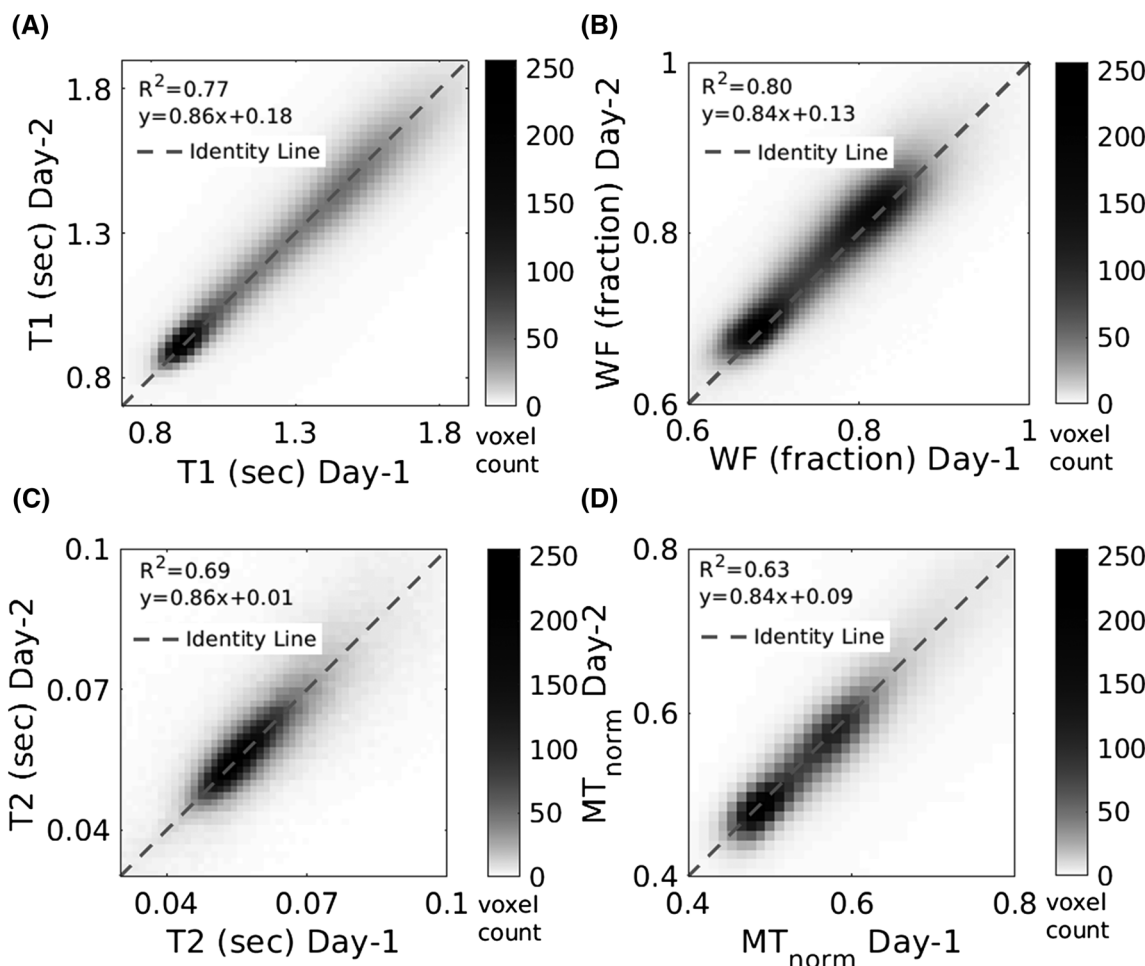


FIGURE 7 Reproducibility of qMRI parameters in a human brain. Relaxation constants were fitted for two scans of the same subject on different days. A-D, the high reproducibility (R^2 range between >0.63 and 0.8) of T_1 , WF, T_2 and MT_{norm} , respectively. The colour of the 2D histogram represents the number of voxels for each corresponding value. Values are around the identity line (dashed line; see inset for linearity equation)

(the non-water fraction), defined as $1 - WF$ (equivalent to the term MTV in the human brain²⁶). Furthermore, we performed Bland–Altman analysis (Figure 8C) and found that the differences between the predicted and the measured WF are an order of magnitude less than the values of WF and close to zero.

In order to further validate our WF estimation, we performed a control experiment (without lipids) and created a set of samples with varying ratios of DDW (H_2O) and D_2O . Since deuterium is an MR-invisible isotope, H_2O/D_2O mixtures can be used to calibrate WF estimations.⁴⁷ Our results indicated an excellent agreement between the MR-estimated WF and the true volume fraction ($R^2 = 0.99$, values are found on the identity line, Figure 8A).

Finally, we tested our assumption that the short T_E used (3.9 ms) did not introduce any T_{2^*} contributions that confounded the estimation of WF in the lipid samples in our system. We compared the WF estimations for T_E of 3.9 ms with the WF estimation for the shortest measured T_E (1.9 ms) and found only a slight difference (Figure 8D, $R^2 = 0.86$, values centred around the identity line with a slope of 0.95). This result demonstrates a negligible T_{2^*} effect given the liposome sample content and the short T_E used in our experiments.

3.4 | Diffusion of the lipid phantom

To test if the phantom system can also be used for diffusion MRI, we measured the MD and FA for a small subset of the samples. Figure S1A shows the signal images of one diffusion direction for the phantom. Figure S1B shows the MD map for the phantom. It is notable that the diffusion images are heavily distorted for our phantom system and careful manual segmentation is needed. Figure 9 shows an example for Spg

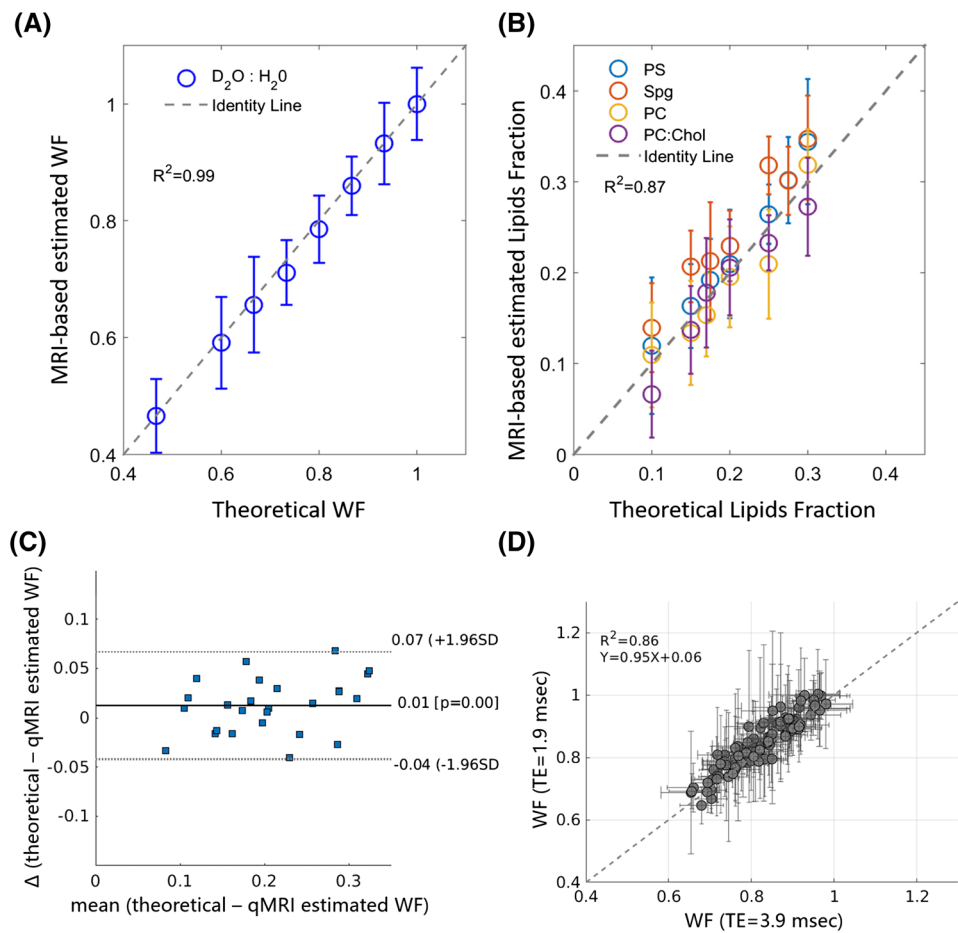


FIGURE 8 Accurate lipid and water fraction estimations in phantom experiments. A, B, the MRI-based estimations (y-axis) agree well with the theoretical estimations (x-axis). Each circle represents the median value across the sample. Lines represent the STD across sample voxels. A, testing the accuracy of water fraction qMRI-based estimations in $\text{H}_2\text{O}-\text{D}_2\text{O}$ mixtures. Each sample is composed of different ratios of H_2O (MRI visible) and D_2O (MRI invisible). The true WF (x-axis) was determined from the fraction of H_2O from the total sample volume (H_2O and D_2O). The MRI-estimated WF (y-axis) is in excellent agreement with the true water volume. B, testing the water fraction estimation accuracy in lipid-H₂O mixtures. Lipid fraction (non-WF) was estimated FOR samples with liposome-H₂O mixtures that have different lipid volume fractions. The true lipid fraction (x-axis) was determined using the theoretical volume of the lipid molecules taken from the literature, and agrees well with the qMRI-based estimated non-WF ($1 - \text{WF}$) (y-axis). The theoretical WF estimation does not account for water loss during the manufacturing process. PS, PC, Spg and PC:Cholesterol represent the phospholipid names (see methods), where PC:Cholesterol is in the ratio of 3:1 by weight. C, Blant-Altman analysis. y-axis is Δ which is the difference between the theoretical and the qMRI estimated WF. x-axis is the average between the theoretical and the qMRI estimated WF. The thick black line is the mean of the differences and the dashed lines are ± 1.96 standard deviation. D, Examining the T₂*contribution to WF estimations from a VFA-T1 map of liposomes. The possible effect of T₂* on WF is calculated from a multi-echo scan. Each point represents the WF. The horizontal and vertical lines represent the median absolute deviation across sample voxels. Comparison between the estimation of WF by the VFA (using TE = 3.9 ms) to WF values calculated using VFA TE (using TE = 1.9 ms). Values are around the identity line (dash line, see inset for linearity equation and R^2)

liposome samples with different concentrations. As expected, the MD is maximal for pure water samples and it decreases when the lipid concentration increases. In contrast, we found that FA values were close to zero and not affected by concentration.

3.5 | Sensitivity to lipid type

Early NMR studies by Kucharczyk et al²² demonstrated that qMRI parameters are sensitive to the type of lipid. In order to validate this sensitivity in our system, we used a clinical MRI system to compare the T_1 , T_2 and MT_{norm} parameters of PC, PC:cholesterol, PS, Spg and PI:PC (Figure 10). As the system provides estimates of the WF of the samples, we will be able to study the qMRI parameters of different lipid types, irrespective of their concentration. As expected, in cases where all samples were made at similar concentrations we also measured similar WF values (Figure 10A). Importantly, these samples with the same WF values have different qMRI parameters for different lipids (Figure 10B).

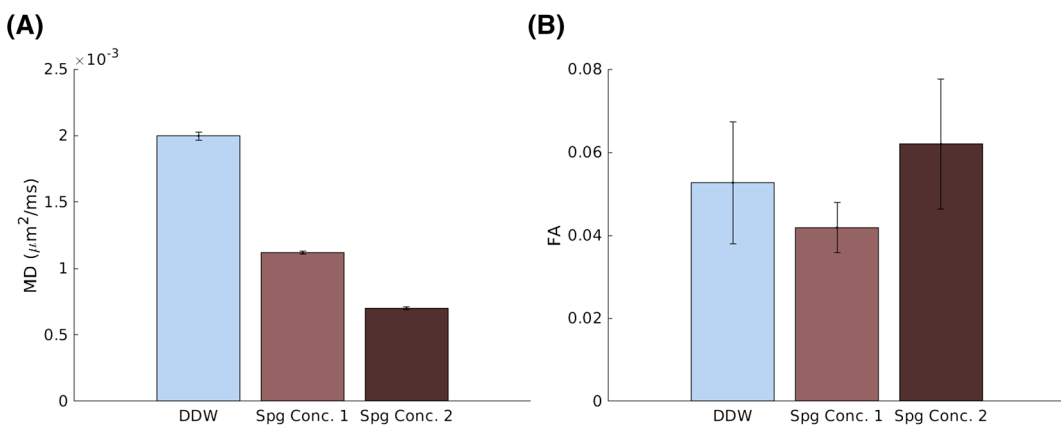


FIGURE 9 Diffusion measurements. A, MD measurements of three samples. DDW is a pure water sample; Spg Conc. 1 and Spg Conc. 2 are two Spg liposome samples (Conc. 2 has higher liposome concentration than Conc. 1). B, FA measurements of three samples. The contents of the samples are identical to those in (A)

4 | DISCUSSION

Quantifying the contribution of lipids and macromolecules to the qMRI parameters is key to understanding *in vivo* human imaging. This study describes the development and validation of a biologically relevant liposome phantom system. The system enables control of the lipid composition and concentration, and provides a reliable measure of the contribution of various lipids to qMRI parameters. In this work, we used non-water volume fractions of 5%–40% (the percentage of lipids in water by volume), which are biologically relevant, and resemble the values found in the grey and white matter of the brain.¹⁰

An important feature of the system is the homogenous agar-Gd surrounding the cuvettes, which allows for correction of the qMRI measurements of the liposome samples for the different spatial inhomogeneities in VFA scans. After correction, the distributions of T_1 and PD values within the samples were not influenced by slice position, indicating that our liposome samples were homogeneous, with minimal amounts of unwanted precipitates or air bubbles. Repeated scans and experiments revealed that the STDs in our system were at least one order of magnitude smaller than the values of estimated parameters both within the samples ($CV < 0.09$) and between the scans ($CV_{\text{scan-rescan}} < 0.06$). In some cases, we identified minor variations that may be due to temperature fluctuations, changes in the structure of the liposomes with time or imperfections in post-processing (such as imperfect ROI segmentation). Interestingly, samples with greater WF had higher variability (Figure 5), as described previously in the literature.⁴⁵

For MT analysis, we employed the MT_{norm} calculation, with 700 Hz off-resonance frequency selected as our MT_{on} signal. In our system, the water samples gave a MT_{norm} value of 1 at ~700 Hz with an MT power flip angle of 220°. Therefore, this off-resonance pulse allowed us to estimate the MT contributions in the lipid samples while minimizing the direct effect of water.

The z-spectrum values of the liposome system are found in a different range from the typical human scan but are similar to other phantom studies.⁴⁸ It is important to note that the z-spectrum range depends on the MT power angle used and the substrate measured.^{48,49} Indeed, in our scan both the power angle and substrate are different from those for the *in vivo* human brain.

For T_2 mapping, we relied on the EMC approach. Our results verified that this fitting technique generated reliable T_2 maps.

Finally, we also excluded possible B_0 inhomogeneity and orientation dependence from the qMRI maps. In addition, we show consistency between the slices of the phantom with a typical SNR for the measurements.

The reproducibility of the system suggests that this phantom system can be further used to compare contributions of lipids manufactured and scanned at different times (Figure 5). We suggest that this lipid phantom system could also be used to test a variety of qMRI models⁵⁰ and novel techniques.^{51,52}

Employing these protocols allowed us to accurately and reliably measure the qMRI parameters of the lipid samples. Importantly, we were able to show that the system is applicable to measurements in humans, thereby providing a useful controlled model system to study the effects that these lipids have on qMRI parameters. The reproducibilities of the parameters from repeated scans of human subjects were comparable to those obtained from the lipid phantoms, with high R^2 and small $CV_{\text{scan-rescan}}$. In addition, similar ranges of the qMRI parameter values were obtained in lipid phantoms and the human brain. However, factors such as noise measurement in the ventricle regions, motion and imperfect registration affected only the reproducibility of measurements in the human brain. An additional source of variability in the human measurements is that, while in the phantom system we average all the voxels in a homogenous cuvette, in the human brain it is necessary to test the voxel to voxel agreement. Those factors can explain why the R^2 and $CV_{\text{scan-rescan}}$ of the phantom scans were higher. Nevertheless, we find good agreement (in

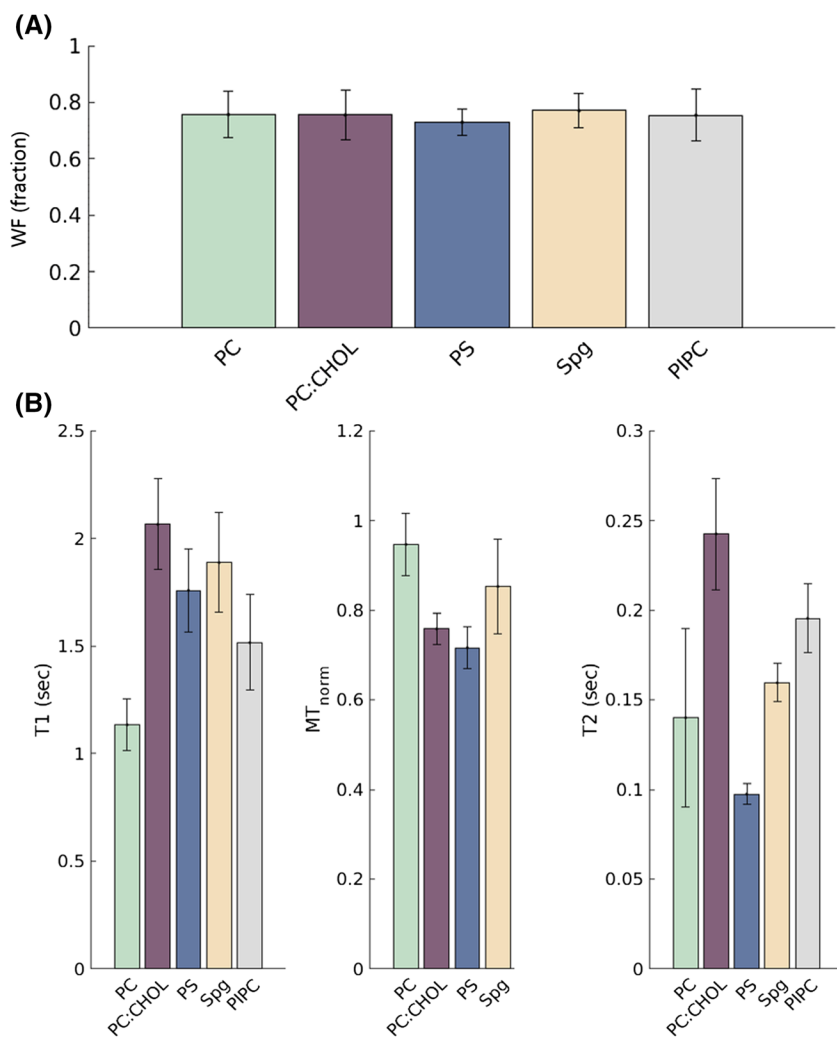


FIGURE 10 Sensitivity of qMRI parameters to lipid type. A, we prepared five liposome samples, each made of a different lipid type, but with similar WF values. B, the qMRI parameters T_1 , T_2 and MT_{norm} for the samples shown in a. PC: Cholesterol is in the ratio of 3:1 by weight, and PI: PC is in the ratio of 1:8 by weight (no data for MT_{norm})

values and reproducibility) between the human and phantom scans. Furthermore, in the supporting literature we also found the same range of reproducibility of these qMRI methods for humans.^{26,53-56}

We validated that the quantitative WF maps reflect the true water. We also show that MTV ($1 - WF$) is equivalent to the lipid volume fractions of the prepared samples (Figure 8). In the case of liposomes, the T_2^* contribution to the WF estimation was negligible (Figure 8D). The accuracy of these WF estimations enables a reliance on the qMRI measurements of WF. In particular, it means that the phantom system can be used for other samples with unknown WF.

It is interesting to note that T_1 and T_2 were suggested as a measure of PD.¹ However, T_1 and T_2 parameters are only proportional to PD and their proportionality is not specific. We and others have shown that this proportionality changes when the molecular composition of the tissue changes.⁵⁷ For this reason, T_1 and T_2 are not a true estimation of PD. Therefore, we find that the method for extracting PD' from the spoiled gradient-echo signal equation together with an approach method to normalize PD' to WF is more precise.

Finally, we would like to emphasize that we assume that the protons of the phospholipids we used (and are found in brain cell membranes) do not affect PD estimations. This is because the T_E that was used is long enough relative to the very short T_2 of those protons (μ s).⁴⁰ This is in contrast to lipids (fat, in the majority of non-brain regions) that have much longer T_2 and would affect the PD estimation. Figure 8B shows the comparison of the theoretical WF (given the phospholipid volume) and the qMRI estimation of WF ($R^2 = 0.87$). Furthermore, a Bland-Altman analysis (Figure 8C) shows a mean difference close to zero (Δ is also an order of magnitude less than the values of WF) and provides support for this assumption. Nevertheless, we cannot entirely exclude marginal effects of the non-water protons to our estimations.

Establishing a stable but flexible MRI phantom system for lipids has great potential for investigating the contribution of lipid composition to qMRI parameters. Figure 10 shows that changing the liposomes' lipid composition affects the qMRI parameters. Earlier studies^{22,30} introduced the notion that a difference between lipids can affect the relaxation measured with NMR. A main contribution of this study is to establish a phantom system that uses qMRI approaches that are similar to the one used for humans. In addition to the earlier studies, our approach incorporated estimations for the WF of the samples and not only relaxation.

Our liposome system provides a useful tool to model how water relaxation is influenced by different molecular environments. Importantly, we argue that knowing the WF may enable the disentanglement of the WF contribution to the qMRI parameters from the physical-chemical factors of interest. In a recent study, we showed that taking both the WF and the relaxation values of a substrate (e.g. lipid and proteins) allows us to identify its unique relaxivity.⁵⁷ In Figure 10 we show an example of lipid samples that have the same WF but different relaxation values.

Figure 9 shows that not only relaxation but also the diffusivity (MD) is affected by the fraction of water; this is in agreement with theory.⁴² In contrast, since our lipid samples are round with no clear directionality, the FA was not sensitive to the lipid content.

Another great advantage of the liposome phantom system is the ability to change the spatial organization of the samples. For example, sonication can produce a controlled change in the distribution of liposome size³³ and thereby enable an examination of water-lipid surface interactions and their effects on relaxation. Furthermore, it is possible to use such a liposome system when modelling the lipid contribution for imaging of brain pathological states. Such a model may incorporate not only lipid but also ions, sugars and proteins. A good example can be found in the recent work of Shaharabani et al,⁵⁸ where they synthesized myelin-like lipid samples corresponding to healthy and multiple sclerosis cell membranes. It would be interesting to incorporate these myelin-like lipid samples within our qMRI phantom system.

It is important to note that any lipid phantom system is much simpler than the complex cell membrane. Nevertheless, washing the lipids from a post mortem brain to leave only the proteins depletes most of the MRI contrast.¹⁶ We predict that integrating proteins into the liposome system together with the ability to change its spatial organization⁵⁸ will have great value for the future understanding of the MRI signal in complex biological systems.

Stability is an important aspect for phantom systems. We showed it is possible to use the same sample for over a period of two weeks and receive similar qMRI values (Figure S7). A literature review shows a set of additional protocols to extend the shelf life of liposomes for example, as follows.

- a. Optimization of the manufacturing process (e.g. freeze-thaw cycle⁵⁹).
- b. Optimal mixture content (e.g. cholesterol rich samples²⁴).
- c. Storage conditions (e.g. minimal O₂, optimal temperature²⁴ as well as sample dehydration using lyophilizer⁶⁰).
- d. Adding a preservative to the lipid samples²⁷.

While each of these steps may dramatically increase the shelf life of the samples, their use for MRI analysis requires further research.

In conclusion, we have successfully developed a biologically relevant liposome phantom system accompanied by an analysis pipeline that is compatible with a human qMRI protocol. This phantom system allows the content to be controlled and enables the reliable and accurate measurement of the contribution of various lipids to multiple qMRI.

ACKNOWLEDGEMENT

This work was supported by the ISF Grant (no 0399306) awarded to A.A.M. We thank the Rudin foundation for their supporting scholarship (O. S.).

We thank Roey Schurr, Batsheva Weisinger and Jonathan Bain for helpful comments on this manuscript.

We thank Dr Adi Pais for her help in designing scan protocols. We thank Joohoon Ha for his help with the experiments. We thank Shir Filo for her help with the human scan and analysis. We thank Menachem Gutman, Eti Nachliel, Assaf Friedler and Mattan Hurevich with their help with liposome formation and the use of their laboratory. We thank Noam Ben-Eliezer for his help with the T₂ analysis.

FUNDING INFORMATION

This work was supported by an ISF grant (0399306).

ORCID

Oshrat Shtangel  <https://orcid.org/0000-0003-1368-3288>

REFERENCES

1. Cercignani M, Dowell NG, Tofts PS (Eds). *Quantitative MRI of the Brain: Principles of Physical Measurement*. 2nd ed. Boca Raton, FL: CRC Press.
2. Dinse J, Hartwich N, Waehnert MD, et al. A cytoarchitecture-driven myelin model reveals area-specific signatures in human primary and secondary areas using ultra-high resolution in-vivo brain MRI. *Neuroimage*. 2015;114:71-87. <https://doi.org/10.1016/j.neuroimage.2015.04.023>
3. Laule C, Vavasour IM, Kolind SH, et al. Magnetic resonance imaging of myelin. *Neurotherapeutics*. 2007;4(3):460-484. <https://doi.org/10.1016/j.nurt.2007.05.004>
4. Helms G, Draganski B, Frackowiak R, Ashburner J, Weiskopf N. Improved segmentation of deep brain grey matter structures using magnetization transfer (MT) parameter maps. *Neuroimage*. 2009;47(1):194-198. <https://doi.org/10.1016/j.neuroimage.2009.03.053>
5. Whittall KP, Mackay AL, Graeb DA, Nugent RA, Li DKB, Paty DW. *In vivo* measurement of T₂ distributions and water contents in normal human brain. *Magn Reson Med*. 1997;37(1):34-43. <https://doi.org/10.1002/mrm.1910370107>

6. Stüber C, Morawski M, Schäfer A, et al. Myelin and iron concentration in the human brain: a quantitative study of MRI contrast. *Neuroimage*. 2014;93(P1):95-106. <https://doi.org/10.1016/j.neuroimage.2014.02.026>
7. Tournier JD, Calamante F, Gadian DG, Connelly A. Direct estimation of the fiber orientation density function from diffusion-weighted MRI data using spherical deconvolution. *Neuroimage*. 2004;23(3):1176-1185. <https://doi.org/10.1016/j.neuroimage.2004.07.037>
8. Keenan KE, Ainslie M, Barker AJ, et al. Quantitative magnetic resonance imaging phantoms: a review and the need for a system phantom. *Magn Reson Med.* 2018;79(1):48-61. <https://doi.org/10.1002/mrm.26982>
9. Fieremans E, Lee H-H. Physical and numerical phantoms for the validation of brain microstructural MRI: a cookbook. *Neuroimage*. 2018;182:39-61. <https://doi.org/10.1016/J.NEUROIMAGE.2018.06.046>
10. Svennerholm L, Boström K, Jungbjer B, Olsson L. Membrane lipids of adult human brain: lipid composition of frontal and temporal lobe in subjects of age 20 to 100 years. *J Neurochem*. 1994;63(5):1802-1811. <https://doi.org/10.1046/j.1471-4159.1994.63051802.x>
11. Naber D, Korte U, Krack K. Content of water-soluble and total proteins in the aging human brain. *Exp Gerontol*. 1979;14(2):59-63. [https://doi.org/10.1016/0531-5565\(79\)90010-X](https://doi.org/10.1016/0531-5565(79)90010-X)
12. Samorajski T, Rolsten C. Age and regional differences in the chemical composition of brains of mice, monkeys and humans. *Prog Brain Res*. 1973;40(C):253-265. [https://doi.org/10.1016/S0079-6123\(08\)60692-5](https://doi.org/10.1016/S0079-6123(08)60692-5)
13. Markesberry WR, Ehmann WD, Alauddin M, Hossain TIM. Brain trace element concentrations in aging. *Neurobiol Aging*. 1984;5(1):19-28. [https://doi.org/10.1016/0197-4580\(84\)90081-2](https://doi.org/10.1016/0197-4580(84)90081-2)
14. Söderberg M. Lipid compositions of different regions of the human brain during ageing. *J Neurochem*. 1990;415-423.
15. Meer G, Voelker D, Feigenson G. Membrane Lipids: Where they Are and how they Behave. *Nat Rev Mol Cell Biol*. 2009;9(2):112-124. <https://doi.org/10.1038/nrm2330.Membrane>
16. Leuze C, Aswendt M, Ferenczi E, et al. The separate effects of lipids and proteins on brain MRI contrast revealed through tissue clearing. *Neuroimage*. 2017;156:412-422. <https://doi.org/10.1016/j.neuroimage.2017.04.021>
17. Koenig H. Cholesterol of myelin is the determinant of gray-white contrast in MRI of brain. *Magn Reson Med*. 1991;20(2):285-291.
18. Seeger U, Klose U, Mader I, Grodd W, Nägele T. Parameterized evaluation of macromolecules and lipids in proton MR spectroscopy of brain diseases. *Magn Reson Med*. 2003;49(1):19-28. <https://doi.org/10.1002/mrm.10332>
19. Tugnoli V, Tosi MR, Tinti A, Trinchero A, Bottura G, Fini G. Characterization of lipids from human brain tissues by multinuclear magnetic resonance spectroscopy. *Biopolym Biospectrosc Sect*. 2001;62(6):297-306. <https://doi.org/10.1002/bip.10005>
20. Kreis R, Ernst T, Ross BD. Development of the human brain: in vivo quantification of metabolite and water content with proton magnetic resonance spectroscopy. *Magn Reson Med*. 1993;30(4):424-437.
21. Ceckler TL, Wolff SD, Yip V, Simon SA, Balaban RS. Dynamic and chemical factors affecting water proton relaxation by macromolecules. *J Magn Reson*. 1992;98(3):637-645.
22. Kucharczyk W, Macdonald P, Stanisz G, Henkelman M. Relaxivity and magnetization transfer of white matter at MR imaging: importance of cerebrosides and pH. *Radiology*. 1994;192(2):521-529.
23. Fralix TA, Ceckler TL, Wolff SD, Simon SA, Balaban RS. Lipid bilayer and water proton magnetization transfer: effect of cholesterol. *Magn Reson Med*. 1991;18(1):214-223. <https://doi.org/10.1002/mrm.1910180122>
24. Monteiro N, Martins A, Reis RL, Neves NM. Liposomes in tissue engineering and regenerative medicine. *J R Soc Interface*. 2014;11(101):20140459-20140459. <https://doi.org/10.1098/rsif.2014.0459>
25. Mezer A, Rokem A, Berman S, Hastie T, Wandell BA. Evaluating quantitative proton-density-mapping methods. *Hum Brain Mapp*. 2016;37(10):3623-3635. <https://doi.org/10.1002/hbm.23264>
26. Mezer A, Yeatman JD, Stikov N, et al. Quantifying the local tissue volume and composition in individual brains with magnetic resonance imaging. *Nat Med*. 2013;19(12):1667-1672. <https://doi.org/10.1038/nm.3390>
27. Akbarzadeh A, Rezaei-Sadabady R, Davaran S, et al. Liposome: methods of preparation and applications. *Liposome Technol*. 2013;6(II):102. <https://doi.org/10.1017/CBO9781107415324.004>
28. Loosley-Millman ME, Rand RP, Parsegian VA. Effects of monovalent ion binding and screening on measured electrostatic forces between charged phospholipid bilayers. *Biophys J*. 1982;40(3):221-232. [https://doi.org/10.1016/S0006-3495\(82\)84477-9](https://doi.org/10.1016/S0006-3495(82)84477-9)
29. Koenig BW, Gawrisch K. Specific volumes of unsaturated phosphatidylcholines in the liquid crystalline lamellar phase. *Biochim Biophys Acta Biomembr*. 2005;1715(1):65-70. <https://doi.org/10.1016/j.bbamem.2005.07.006>
30. Ulrich AS, Watts A. Molecular response of the lipid headgroup to bilayer hydration monitored by 2H-NMR. *Biophys J*. 1994;66(5):1441-1449. [https://doi.org/10.1016/S0006-3495\(94\)80934-8](https://doi.org/10.1016/S0006-3495(94)80934-8)
31. Nagle JF. Theory of the main lipid bilayer phase transition. *Annu Rev Phys Chem*. 1980;31(1):157-196. <https://doi.org/10.1146/annurev.pc.31.100180.001105>
32. Stempak JG, Ward RT. An improved staining method for electron microscopy. *J Cell Biol*. 1964;22:697-701.
33. Lapinski MM, Castro-Forero A, Greiner AJ, Ofoli RY, Blanchard GJ. Comparison of liposomes formed by sonication and extrusion: rotational and translational diffusion of an embedded chromophore. *Langmuir*. 2007;23(23):11677-11683. <https://doi.org/10.1021/la7020963>
34. MATLAB and Statistics Toolbox [computer program]. Release. Natick, MA: MathWorks; 2017b.
35. Yushkevich PA, Piven J, Hazlett HC, et al. User-guided 3D active contour segmentation of anatomical structures: significantly improved efficiency and reliability. *Neuroimage*. 2006;31(3):1116-1128. <https://doi.org/10.1016/j.neuroimage.2006.01.015>
36. Fram EK, Herfkens RJ, Johnson GA, et al. Rapid calculation of T1 using variable flip angle gradient refocused imaging. *Magn Reson Imaging*. 1987;5(3):201-208. [https://doi.org/10.1016/0730-725X\(87\)90021-X](https://doi.org/10.1016/0730-725X(87)90021-X)
37. Barral JK, Gudmundson E, Stikov N, Etezadi-Amoli M, Stoica P, Nishimura DG. A robust methodology for in vivo T_1 mapping. *Magn Reson Med*. 2010;64(4):1057-1067. <https://doi.org/10.1002/mrm.22497>
38. mrQ. <https://github.com/mezera/mrQ>.
39. VISTASOFT. <https://github.com/vistalab/vistasoft>.
40. Horch RA, Gore JC, Does MD. Origins of the ultrashort- T_2 ^1H NMR signals in myelinated nerve: a direct measure of myelin content? *Magn Reson Med*. 2011;66(1):24-31. <https://doi.org/10.1002/mrm.22980>

41. Ben-Eliezer N, Sodickson DK, Block KT. Rapid and accurate T_2 mapping from multi-spin-echo data using Bloch-simulation-based reconstruction. *Magn Reson Med.* 2015;73(2):809–817. <https://doi.org/10.1002/mrm.25156>
42. Basser PJ, Mattiello J, LeBihan D. MR diffusion tensor spectroscopy and imaging. *Biophys J.* 1994;66(1):259–267. [https://doi.org/10.1016/S0006-3495\(94\)80775-1](https://doi.org/10.1016/S0006-3495(94)80775-1)
43. Jenkinson M, Beckmann CF, Behrens TEJ, Woolrich MW, Smith SM. FSL—review. *Neuroimage.* 2012;62(2):782–790. <https://doi.org/10.1016/j.neuroimage.2011.09.015>
44. Avants BB, Tustison N, Song G. Advanced normalization tools (ANTS). *Insight J* 2009. <http://hdl.handle.net/10380/3113>.
45. Chang L-C, Koay CG, Basser PJ, Pierpaoli C. Linear least-squares method for unbiased estimation of T_1 from SPGR signals. *Magn Reson Med.* 2008;60(2):496–501. <https://doi.org/10.1002/mrm.21669>
46. Vesanen PT, Zevenhoven KCJ, Nieminen JO, Dabek J, Parkkonen LT, Ilmoniemi RJ. Temperature dependence of relaxation times and temperature mapping in ultra-low-field MRI. *J Magn Reson.* 2013;235:50–57. <https://doi.org/10.1016/j.jmr.2013.07.009>
47. Neeb H, Ermer V, Stocker T, Shah NJ. Fast quantitative mapping of absolute water content with full brain coverage. *Neuroimage.* 2008;42(3):1094–1109. <https://doi.org/10.1016/j.neuroimage.2008.03.060>
48. Morrison C, Stanisz G, Henkelman RM. Modeling magnetization transfer for biological-like systems using a semi-solid pool with a super-Lorentzian lineshape and dipolar reservoir. *J Magn Reson B.* 1995;108(2):103–113. <https://doi.org/10.1006/jmrb.1995.1111>
49. Henkelman RM, Huang X, Xiang Q-SS, Stanisz GJ, Swanson SD, Bronskill MJ. Quantitative interpretation of magnetization transfer. *Magn Reson Med.* 1993;29(6):759–766. <https://doi.org/10.1002/mrm.1910290607>
50. Stikov N, Boudreau M, Levesque IR, Tardif CL, Barral JK, Pike GB. On the accuracy of T_1 mapping: searching for common ground. *Magn Reson Med.* 2015;73(2):514–522. <https://doi.org/10.1002/mrm.25135>
51. Ma D, Gulani V, Seiberlich N, et al. Magnetic resonance fingerprinting. *Nature.* 2013;495(7440):187–192. <https://doi.org/10.1038/nature11971>
52. Benjamini D, Basser PJ. Magnetic resonance microdynamic imaging reveals distinct tissue microenvironments. *Neuroimage.* 2017;163:183–196. <https://doi.org/10.1016/j.neuroimage.2017.09.033>
53. Weiskopf N, Suckling J, Williams G, et al. Quantitative multi-parameter mapping of R1, PD*, MT, and R2* at 3T: a multi-center validation. *Front Neurolsci.* 2013;7:95. <https://doi.org/10.3389/fnins.2013.00095>
54. Landman BA, Huang AJ, Gifford A, et al. Multi-parametric neuroimaging reproducibility: a 3-T resource study. *Neuroimage.* 2011;54(4):2854–2866. <https://doi.org/10.1016/j.neuroimage.2010.11.047>
55. Deoni SCL, Williams SCR, Jezzard P, Suckling J, Murphy DGM, Jones DK. Standardized structural magnetic resonance imaging in multicentre studies using quantitative T_1 and T_2 imaging at 1.5 T. *Neuroimage.* 2008;40(2):662–671. <https://doi.org/10.1016/j.neuroimage.2007.11.052>
56. McGuire SA, Wijtenburg SA, Sherman PM, et al. Reproducibility of quantitative structural and physiological MRI measurements. *Brain Behav.* 2017;7(9). <https://doi.org/10.1002/brb3.759>
57. Filo S, Shtangel O, Salamon N, et al. Disentangling molecular alterations from water-content changes in the aging human brain using quantitative MRI. *Nat Commun.* 2019;10(1):3403. <https://doi.org/10.1038/s41467-019-11319-1>
58. Shaharabani R, Ram-On M, Avinery R, et al. Structural transition in myelin membrane as initiator of multiple sclerosis. *J Am Chem Soc.* 2016;138(37):12159–12165. <https://doi.org/10.1021/jacs.6b04826>
59. Stark B, Pabst G, Prassl R. Long-term stability of sterically stabilized liposomes by freezing and freeze-drying: effects of cryoprotectants on structure. *Eur J Pharm Sci.* 2010;41(3–4):546–555. <https://doi.org/10.1016/J.EJPS.2010.08.010>
60. Nireesha GR, Divya L, Sowmya C, Venkateshan N, Niranjan Babu M, Lavakumar V. Lyophilization/freeze drying—an review. *Int J Novel Trends Pharm Sci.* 2013;3(4):87–98.

SUPPORTING INFORMATION

Additional supporting information may be found online in the Supporting Information section at the end of this article.

How to cite this article: Shtangel O, Mezer AA. A phantom system for assessing the effects of membrane lipids on water proton relaxation. *NMR in Biomedicine.* 2020;33:e4209. <https://doi.org/10.1002/nbm.4209>